THz biosensing devices: fundamentals and technology

2006 J. Phys.: Condens. Matter 18 S601

(http://iopscience.iop.org/0953-8984/18/18/S07)

INSTITUTE OF PHYSICS PUBLISHING JOURNAL OF PHYSICS: CONDENSED MATTER

J. Phys.: Condens. Matter **18** (2006) S601–S618 doi:10.1088/0953-8984/18/18/S07

THz biosensing devices: fundamentals and technology

M Nagel, M Först and H Kurz

Institute for Semiconductor Electronics, RWTH Aachen University, Sommerfeldstrasse 24, 52074 Aachen, Germany

E-mail: nagel@iht.rwth-aachen.de

Received 31 July 2005
Published 19 April 2006
Online at stacks.iop.org/JPhysCM/18/S601

Abstract

Future success of biological THz technology applications will strongly depend on the development of compact, low-cost and flexible systems. In this work different approaches for THz biosensor systems based on femtosecond lasers are presented. We discuss the technology for generation, transmission and detection of THz signals as well as their application for marker-free biomolecule detection on functionalized surfaces in dry and fluid environments.

1. Introduction

In the past few years THz technology has become increasingly important for biological applications [1]. The THz frequency range is particularly interesting for biosensing applications because numerous characteristic vibrational modes of macro-molecules, like proteins [2] or DNA [3], are located in this part of the spectrum. Therefore, THz probing techniques provide large potential for marker-free biosensing. The energy levels at THz frequencies are low (4 meV at 1 THz) enabling low-invasiveness probing of biological samples. THz probes have recently been applied to identify conformational states of proteins [4], monitor receptor binding events [5] and for DNA analysis [6] and imaging of cancerous tissue [7]. Nevertheless, the development of THz biosensing systems is still in an early stage. In this work we address some current technological concepts for THz biosensing: first, we describe the technology for THz generation and detection based on femtosecond lasers, covering recent approaches for high-speed time-domain scanning. The second part of the paper is focused on integrated THz biosensor device concepts.

2. THz generation and detection

Since the early beginnings of femtosecond pulse lasers around 1990 state-of-the-art THz sources were based on the generation of picosecond or sub-ps electromagnetic pulses via the interaction between infrared fs laser pulses and semiconductor device structures. Still now, pulsed THz sources are the workhorse in the majority of ultrafast optics laboratories

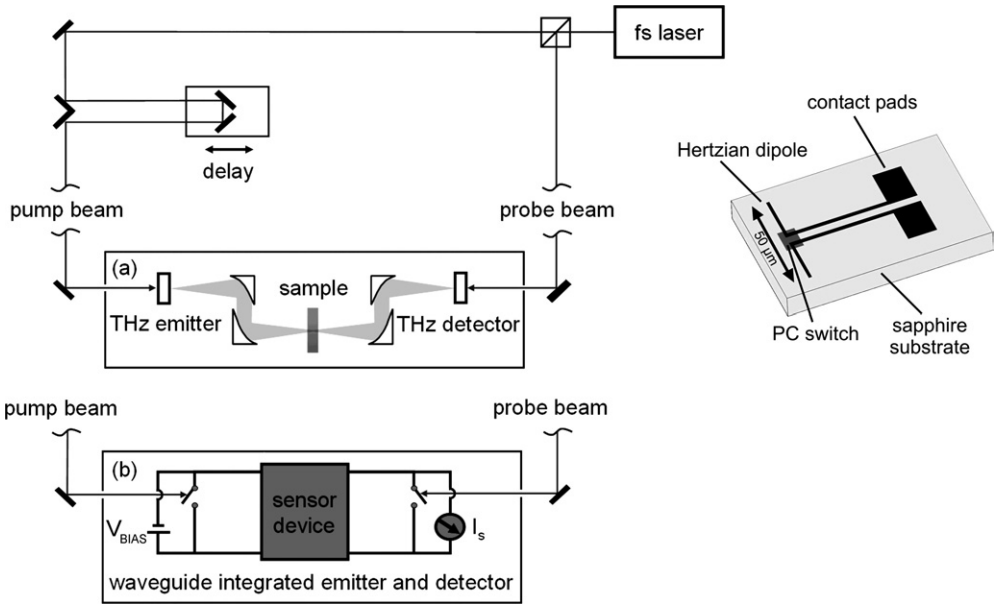

Figure 1. Schematic drawing of two types of time-domain pump/probe measurement set-ups. A femtosecond laser and a delay scanning stage are applied to facilitate generation and time-resolved detection of transmitted THz signals. (a) Quasi-optical variation using propagation of free-space THz radiation generated and detected with photoconductive antennas (see inlay). (b) Equivalent circuit diagram representing a waveguide based scheme using integrated photoconductive switches.

devoted to the field of THz technologies—although the development of single-device THz sources, e.g. continous-wave (cw) quantum cascade lasers, is progressing at enormous speed. For an overview of different types of THz sources we refer to recent review articles by Schmuttenmaer [8] and Dragoman and Dragoman [9].

2.1. Measurement system components

Several methods have been explored to generate THz signal pulses from infrared femtosecond lasers. In particular, for the generation of free space THz radiation, optical rectification in transparent semiconductors (e.g., ZnTe or GaP) [10, 11] and surface depletion field screening in opaque semiconductors (e.g., $In_xGa_{1-x}As$ compounds) [12] were intensively exploited. On the other hand, by making use of the photoconductive effect in Auston switches [13, 14] THz pulses can be generated with the advantage of tailoring the spatial emission characteristics. This latter effect is specifically valuable for the implementation of photoconductive switches into integrated THz sensor devices where THz pulses are directly coupled into specifically designed waveguide structures [15].

The classic implementation of a photoconductive switch into a THz antenna structure is principally sketched on the right-hand side of figure 1: a metallic coplanar stripline terminated by a Hertzian dipole antenna is deposited on top of a photoconductive semiconductor layer. A dc bias voltage V_{bias} on the order of 10–20 V can be applied to the antenna structure via metal wires bonded to contact pads at the end of each strip line. For the generation of THz pulses, a fs laser is focused onto the antenna structure. Typically solid state Ti:sapphire lasers are used for this task; however, much more compact fibre lasers—making costly pumping sources and external water cooling obsolete—are progressively advancing. In the biased gap between the

antenna arms the laser pulses optically excite charge carriers, which are then accelerated by the associated static electric field. Both the photoexcited change in the carrier density $\partial n/\partial t$ and the acceleration of these carriers $\partial v/\partial t$ result in the emission of a THz field E_{THz} via

$$E_{\mathrm{THz}} \propto \frac{\partial}{\partial t} j(t) = q\left(v\frac{\partial n}{\partial t} + n\frac{\partial v}{\partial t}\right), \tag{1}$$

where q is the elementary charge and j the current density. With respect to this relation the requirements to the semiconductor material used are short carrier lifetime and high carrier mobility. These are excellently fulfilled by low-temperature-grown (LT-) GaAs, which is probably the most commonly applied semiconductor in THz PC switches [16, 17]. In this material, molecular beam epitaxy growth at comparably low temperatures below 250 °C and subsequent high-temperature annealing above 800 °C result in the formation of metallic As precipitates. These clusters act as ultrafast sub-picosecond trapping centres of optically excited charge carriers in the centre of the electronic bandgap between valence and conduction bands [18, 19] while the LT-GaAs carrier mobility is still larger than 2000 $\mathrm{cm^2\ V^{-1}\ s^{-1}}$ [20].

PC switches as described here can also be used for the detection of THz pulses. Again, femtosecond laser pulses are employed to optically inject charge carriers into the semiconductor layer. In contrast to the generation process, however, the antenna arms are not biased. Instead, the current I_{sig} is measured by a high-speed transimpedance amplifier and standard data acquisition hardware.

To time-resolve the detection of a THz field, optical pump/probe techniques are applied which are well established in the field of femtosecond spectroscopy. The standard principle of a time-domain THz spectroscopy set-up is schematically shown in figure 1. A single femtosecond laser system provides both pump and probe pulse trains for THz generation and detection. The pump pulse train is used for the excitation of sub-ps electrical pulses as described above at a first PC switch. The probe pulses are time-delayed by a mechanical delay stage before injecting carriers into the second PC switch to allow for the time-resolved THz pulse detection. An inherent advantage of this time-domain scanning technique is the direct measurement of the transient electric THz field in amplitude *and* phase. For this reason, after transmission through a sample material of interest the real *and* imaginary parts of the complex refractive index of this material can be determined simultaneously within one measurement—for all frequencies covered by the broadband THz pulse. In addition, this coherent type of detection eliminates background noise from thermal incoherent blackbody radiation which is not negligible in the THz frequency range. The pump/probe scheme can be applied to quasi-optical set-ups using propagation of free-space THz radiation or to waveguide-based integrated transceiver systems on a chip as sketched and denoted with (a) and (b), respectively, in figure 1.

2.2. Time-domain scanning concepts

2.2.1. Opto-mechanical delay scanning. For the majority of THz time-domain scanning systems, the time delay between pump and probe pulses is achieved by mirrors or retro-reflectors mounted onto motorized translation stages. In this case large time delays up to the order of nanoseconds can be scanned with femtosecond time resolution, which is important for THz sensing applications requiring high frequency resolution. However, scanning rates are fairly limited: the transient THz field is recorded step-by-step at subsequent time delay points. For sufficiently high signal-to-noise (SNR) ratios the signal is averaged at every single delay point by lock-in detection techniques.

Alternatively, motorized translation stages can be replaced by vibrating membranes, which enable delay scanning at frequencies of up to 100 Hz. In this case, data acquisition is accomplished in the so-called fast-scan mode where outstanding SNR increase at drastically

reduced acquisition times is achieved by averaging over the on-line recorded transient signals [21]. The drawback of this technique, however, is the limited amplitude of such vibrating delay lines which at maximum is on the order of one hundred picoseconds. Nevertheless, this is a sufficiently long time window for a multitude of THz applications.

Only a few approaches have been introduced to close the gap between high scan rates and simultaneously large time delays. Using the femtosecond Fourier-transform pulse shaping technique (a combination of gratings and a spatial light modulator), an increase of the scanning rate up to 400 Hz was demonstrated but the maximum time delay of this technique was still limited to below the hundred picosecond range [22]. A kilohertz delay scanning line for fast-scan data acquisition was realized by employing wedged prisms lined up on a rotational wheel, but again nanosecond time delay scanning could not be demonstrated [23]. The most promising mechanical delay stage was recently introduced by Xu and Zhang [24]. They reported a circular involute stage with a rotating mirror pair for high-repetition (up to some hundred Hz) nanosecond delay range scanning for high-resolution terahertz time-domain spectroscopy and general optical pump/probe experiments.

2.2.2. Asynchronous optical sampling for high-speed scanning. An alternative to overcome the limitations of mechanical delay stages is the use of *two* femtosecond lasers to deliver pump and probe pulses in a time-resolved experiment. In this case the time delay is scanned by means of slightly different, but stabilized pulse repetition rates without the need for moving mechanical components. This sampling technique is called asynchronous optical sampling (ASOPS) and was originally introduced in the late 1980s by use of state-of-the-art femtosecond lasers with repetition rates in the 100 MHz range [25, 26]. In 2004, Keilmann *et al* demonstrated a time-domain mid-infrared frequency comb spectrometer which is based on a related method [27].

The available scan window of the ASOPS approach is given by the pulse-to-pulse spacing of the 'pump' laser (i.e., the inverse of its repetition rate f_R), whereas the scan rate is determined solely by the difference between the two lasers' repetition rates Δf_R. This detuning can be set to any value from a few hundred hertz to several megahertz, thus providing the means for a major reduction in measurement time. Further advantages of ASOPS compared with standard pump–probe techniques based on a single fs laser are the absence of changes in optical spot size and of pointing instabilities (especially at long time delays), and the elimination of noise caused by moving mechanical components. An upper limit to the scan rate is imposed by the time resolution desired for the specific application. The time resolution τ of the ASOPS technique is principally governed by the femtosecond laser repetition rates and their detuning via

$$\tau = \frac{1}{f_R} - \frac{1}{f_R - \Delta f_R} \approx \frac{\Delta f_R}{f_R^2}. \tag{2}$$

From this relation it is obvious that the use of femtosecond lasers with higher repetition rates in the GHz range becomes increasingly favourable if higher time resolutions are required. Further attention has to be paid to the available bandwidth of the detection and data-acquisition electronics, and the stability of the laser repetition rates. At a given detection bandwidth F and a desired time resolution τ, the scanning rate Δf_R is further restricted according to $\Delta f_R \leqslant \tau f_R F$ [28]. But again, this relationship favours the use of femtosecond lasers with increased repetition rates. To reduce timing jitter in the data acquisition process, i.e. to reduce slight deviations from a chosen scan rate, the cavity lengths of the two lasers have to be actively stabilized. This can be accomplished by the use of one piezo-driven mirror in each laser resonator controlled by separate phase-locked loops (PLLs).

Very recently, we have demonstrated the first application of the ASOPS approach in the field of time-domain THz scanning [29]. By employing two actively stabilized GHz repetition

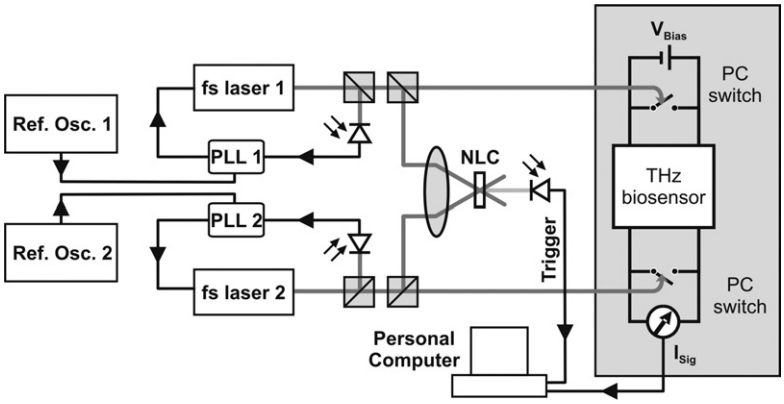

Figure 2. Experimental set-up of the ASOPS approach as recently published by Janke *et al* [29]. The set-up comprises two fs lasers at a 1 GHz repetition rate and an integrated THz biosensor device. The laser repetition rates are locked to two synthesizers (sharing a common time base) by use of two PLLs. The trigger signal for the data-acquisition system is generated by use of a nonlinear $LiIO_3$ crystal (NLC).

rate femtosecond lasers (model GigaJet, Gigaoptics, Germany) [30] at a scanning rate of 5 kHz and a scanning window of 1 ns, the read-out time of an integrated THz resonator could be reduced by a factor of 20 as compared to conventional time delay scanning via lock-in detection and a motorized translation stage. The experimental set-up of this experiment is schematically plotted in figure 2. The repetition rates of the femtosecond lasers are measured by high-speed photodiodes and actively stabilized by locking them to external reference oscillators with a difference frequency of 5 kHz. A trigger signal for the data acquisition system (model Saturn Fast Scan, AMO, Germany) is provided by detecting the cross-correlation signal between the lasers in a nonlinear lithium iodate ($LiIO_3$) crystal.

3. Biosensing with THz technology

THz propagation can be accomplished by quasi-optical techniques using transmission of THz free-space radiation or by waveguide-based techniques. Quasi-optical THz-systems are widespread since they offer a simple method for low-loss and broad-band THz transmission. However, these measurement systems are rather bulky because large collimators with focal lengths of some centimetres have to be used. Additionally, water vapour has to be excluded from the THz beam path in order to avoid water absorption lines in the transmitted THz signal spectrum. Using waveguide technology with integrated generation/detection devices, on the other hand, THz spectroscopy systems can be made very compact with only sub-millimetre path lengths. Waveguide-based THz transmission is also totally insensitive to environmental water vapour using completely screened waveguides. However, quasi-optical THz systems are still dominating the field. One reason might be that practicable waveguides with appropriate performance for broad-band THz transmission have become available only recently [31, 32].

3.1. Waveguide-based integrated biosensing devices

The first dedicated THz biosensor demonstrated has been applied to DNA detection [33]. Common methods for identifying polynucleotide sequences are based on detecting hybridization of unknown DNA molecules to complementary immobilized probe molecules with a known base sequence. Binding event detection is largely based on fluorescent labelling

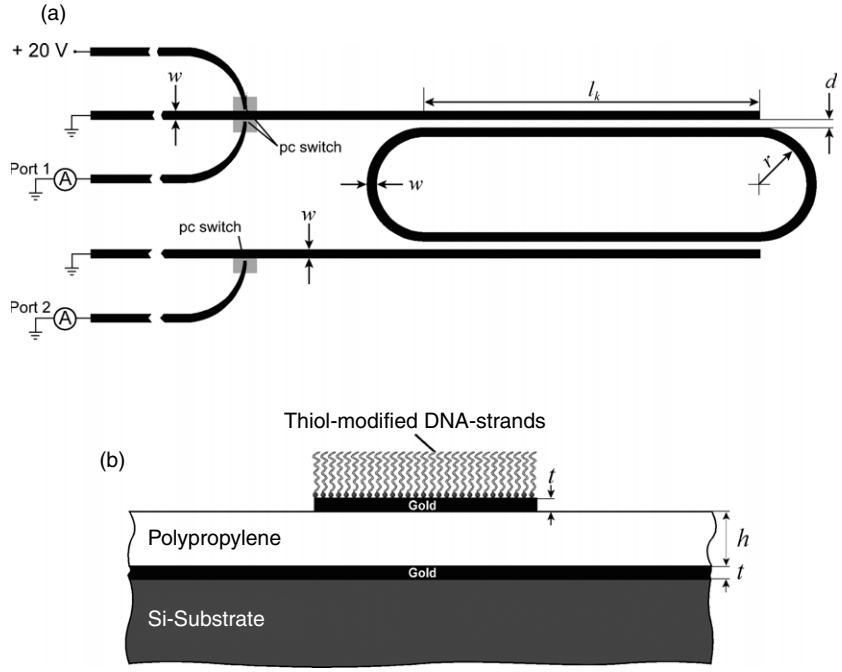

Figure 3. Scheme of the THz ring-resonator (top-view (a) and cross-section (b)) functionalized as sensor for DNA analysis with gold signal conductors (■) and photoconductive LT-GaAs switches □. The geometrical dimensions are $w = 30\ \mu$m, $l_k = 1.5$ mm, $r = 225\ \mu$m and $d = 40\ \mu$m. The length of the branch lines is 29 mm.

and optical localization of the target DNA molecules. Label-based probing has enabled high-throughput DNA detection with sensitivities reaching single-molecular levels. However, large interest exists in the development of label-free methods, due to the costs and the invasiveness associated with label-based probing [34]. Since a multitude of intrinsic THz resonances are associated with inter-backbone excitations of DNA molecules (propeller-twist, hydrogen-bond breathing, base-roll and base-shift vibrational modes) [3, 35] it stands to reason to try using THz-probing technologies for label-free detection of DNA binding states. With a quasi-optical detection scheme DNA molecules with a length of 5.4 kb deposited and dried on a sapphire substrate have been investigated. A broadband (0.4–2.2 THz) higher real and imaginary refractive index was observed for hybridized DNA molecules in comparison to the denatured state [36]. Despite its proof-of-principle relevance, this work also revealed a major drawback of the applied free-space transmission configuration—the requirement of large amounts of DNA for yielding reliable results. Waveguide-based resonant detection, as will be addressed in the following, drastically enhances the analytic sensitivity by orders of magnitude and reduces the DNA material requirements down to femtomolar levels.

3.1.1. On-chip molecule detection at functionalized planar waveguide sensors. The first sensor configuration we want to discuss here is based on thin-film microstrip (TFMS) line waveguides building a ring-resonator device [37] as sketched in figure 3. The resonance frequencies of ring resonators are determined by

$$f_{r,n} = n\frac{c_0}{l_r\sqrt{\varepsilon_{\text{eff}}}}, \tag{3}$$

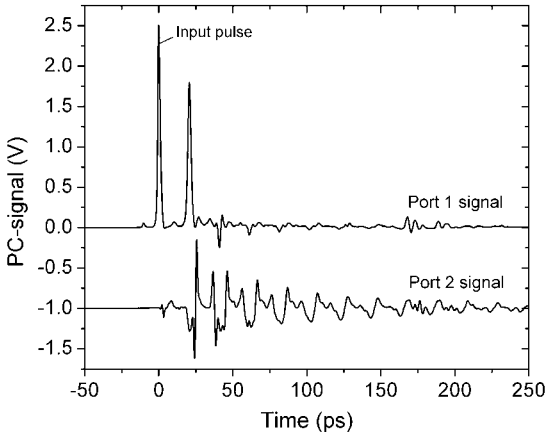

Figure 4. Time-resolved signals measured at port 1 and port 2 of the unloaded resonator. The reflected signal of the resonator arises 14 ps after the excitation pulse in the signal probed at port 1. The data probed at port 2 contains the signal transmitted through the resonator. It has been shifted for clarity by −1 V.

where n is a multiple integer (order), c_0 the speed of light, l_r the average circumference of the resonator and ε_eff the effective permittivity of the TFMS line. At frequencies f_r, where the resonance condition is fulfilled, the number of transmission events through the sample is approximately multiplied by the quality factor $Q = f_\mathrm{r}/\Delta f_\mathrm{r}$ of the resonator. Δf_r is defined as the 3 dB bandwith of the resonator pass-band. The ring resonator amplifies the interaction between the THz signal and the probed sample in a controlled and efficient way. The sensitivity is increased at frequencies $f_{\mathrm{r},n}$, but decreased within the non-resonant frequency ranges. The complex effective permittivity of the TFMS lines and with it the characteristic parameters of the resonator, such as resonance frequency or quality factor, is altered in dependence on the dielectric properties and amount of sample material brought to the resonator.

For optoelectronic generation and detection of THz signals photoconductive switches are integrated into the sensor. The switches are made of thin 800 nm LT-GaAs as photoconductive material. TFMS lines with a self-adhesive polypropylene (PP) film as dielectric are used as waveguides [31]. The cross section of the TFMS lines is depicted in figure 3(a). A silicon wafer with a mass metallization on top serves as the substrate. A 57 μm thick polypropylene dielectric layer is attached to the substrate through a co-polymer acrylate adhesive layer. The signal line is defined from a Ti/Au layer on top by optical lithography. All metal layers have a thickness $t = 0.5$ μm. Electrical sub-ps pulses are excited at 20 V biased PC switches by optical pulses of a 780 nm Ti:sapphire laser operating at a repetition rate of 78 MHz. The electric signal is guided along the TFMS lines and through the resonator. The reflected and transmitted signals from the resonator are sampled with additional PC switches by time delayed optical pulses (see above) and measured at port 1 and port 2, respectively, as sketched in figure 3.

Time-domain data measured at an unloaded resonator are shown in figure 4. The signal probed at port 1 exhibits the generated input signal for time delay $t < 14$ ps. For $t > 14$ ps the signal reflected from the resonator is detected. The second pulse at $t = 20.3$ ps is the reflection of the input pulse from the open end of the coupling section at the resonator input. The signal sampled at port 2 exhibits strongly modulated decaying oscillations with a superposition of different frequency components. The time range available for characterization is restricted by the back reflection of the open-ended branch lines with a length of 29 mm. This signal

is observed at 260 ps time delay. The design of the PC switches produces only negligible multiple reflections of the back-reflected signal from the resonator.

In order to use the ring resonator as a sensor for DNA molecule detection its metallic signal line surface is chemically functionalized with single-stranded probe molecules. All binding and hybridization experiments are performed with complementary single-stranded DNA (ssDNA) of 20 base long oligonucleotides with a calculated melting point of 60 °C (MWG Biotech, Ebersberg, Germany). Thiolated molecules with the sequence 5′–HS–$(CH_2)_6$–ACA CTG TGC CCA TCT ACG AG-3′ (probe) serve as capture probes. The hexanethiol modifier ($-(CH_2)_6$–SH) links these molecules to the gold surface of the ring resonators via a stable sulfur–gold linkage (strength of Au–S bond: 40 kcal mol^{-1} [38]). Target molecules can hybridize to these capture probes consisting of complementary ssDNA oligonucleotides with the sequence 5′-TGT GAC ACG GGT AGA TGC TC-(6-FAM)-3′ (target). The fluorescence marker at the 3′-end has been applied to allow additional optical control of the binding process. Aliquot 1 μM solutions of both types of oligonucleotides are hybridized at 50 °C over a period of 12 h in a TE-NaCl buffer solution before chemical binding to the electrodes in order to avoid unspecific attachment of non-saturated ssDNA to the gold or polymer surfaces [39, 40]. The functionalization and test of the sensor is done in five consecutive process steps. Each process step is followed by a measurement monitoring the response of the THz sensor. For further reference the process steps are tagged by abbreviations. The applied process steps are in detail the following.

(a) *Immobilization of dsDNA (Imm. dsDNA).* Immobilization of dsDNA was performed using a procedure described by Herne and Tarlov [39]. Prior to the actual binding process the surfaces of all resonator samples were cleaned by rinsing with acetone, isopropanol and DI water ($\rho \geqslant 18.2$ MΩ; Milli-Q plus, Millipore), 5 min each rinse. After drying in a nitrogen stream thiol-modified dsDNA (1 μM) was attached to the gold surface by dipping the resonator parts of the samples in a buffer solution consisting of 1 M KH_2PO_4 (Merck, Darmstadt) and TE-NaCl for 60 min at room temperature. In order to remove excessive dsDNA and salts contained in the buffer solutions all samples were rinsed extensively with TE-NaCl and DI water and subsequently dried in a nitrogen stream before measurements.

(b) *Denaturation of dsDNA (ssDNA (Ref.) and ssDNA).* Resonator samples bearing dsDNA oligonucleotides were heated in TE-NaCl for 60 min at 60 °C. Extensively rinsing first with TE-NaCl followed by DI water was performed to remove the dehybridized target molecules and buffers. After drying in a nitrogen stream the immobilized probe molecules were left bound to the gold surface.

(c) *On-chip re-hybridization (OCH dsDNA).* The parts of the resonator samples bearing the ssDNA molecule probe were dipped in a TE-NaCl solution containing 1 μM ssDNA target for 60 min at room temperature. 1 mM 6-mercapto-1-hexanol (MCH, Fluka, Buchs (CH)) was added to the solution in order to detach probe ssDNA molecules that may be non-specifically bound to the surface. Due to the higher bond strength of the thiol–gold linkage a stronger affinity of the MCH molecules to the gold surface in comparison to the nucleobases of the ssDNA probe molecules can be expected. As a result the ssDNA side chains are separated from the surface [39]. After re-hybridization all samples were rinsed extensively with TE-NaCl and DI water to remove excessive ssDNA target molecules and buffer salts.

(d) *Control process (Buffer).* In order to estimate and exclude possible influences of the buffer solutions on the measurement signals resonator samples were exposed to pure buffer solutions for 60 min at 50 °C followed by rinsing with DI water.

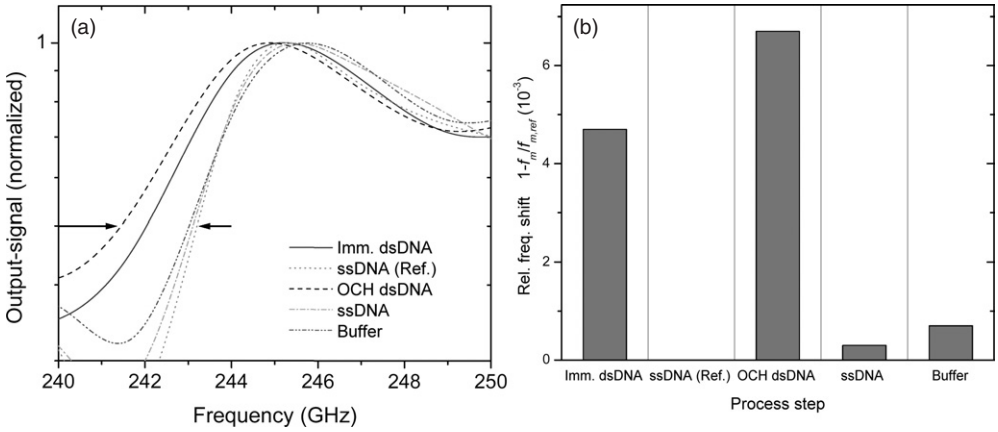

Figure 5. (a) Normalized frequency-dependent output signals of the sensor around 245 GHz for every process step: (1) immobilization of dsDNA (*Imm. dsDNA*), (2) denaturation for an activation of the sensor (*ssDNA Ref.*), (3) on-chip hybridization (*OCH dsDNA*), (4) re-denaturation (*ssDNA*) and (5) control process with pure buffer solution without any DNA (*Buffer*). (b) Corresponding bar chart with relative frequency shifts $r_{\text{shift}} = 1 - f_m/f_{m,\text{ref}}$. f_m is the measured frequency at half output-signal amplitude on the rising edge of the signal. $f_{m,\text{ref}}$ is the frequency accordingly defined as the reference after the process step *ssDNA (Ref.)*.

Now, the application of the functionalized sensor for 20-mer oligo molecule detection is demonstrated. The relative humidity was 20–23% for all measurements. The sensor response to every process step is depicted in figures 5(a) and (b). According to equation (3) the data in figure 5(a) shows the spectral behaviour of the resonance for $n = 5$ and $f_{\text{r}} = 245$ GHz of the ring resonator. For clarity, the amplitude of the output signal is normalized and the measurement points are connected by spline curves. Correspondingly, figure 5(b) exhibits the relative frequency shifts $r_{\text{shift}} = 1 - f_m/f_{m,\text{ref}}$ as bar diagrams, with f_m being the frequency at half of the maximum amplitude of the output signal on the rising edge of the signal. f_m measured after the initial functionalization process *ssDNA (Ref.)* is referred to as $f_{m,\text{ref}}$. The quality factor *and* resonance frequency of the resonator are decreased at hybridization of probe molecules. In combination of both effects there is a distinct shift at the rising edges of the output signals, while the falling edges are rather congruent.

The first two process steps conducted include immobilization of dsDNA molecules at the THz-sensor surface (*Imm. dsDNA*) and subsequent denaturation (*ssDNA Ref.*) leaving only single-stranded immobilized probe molecules at the sensor surface. This second step represents the initialization of the functionalized sensor with $r_{\text{shift}} = 0$. Denaturation leads to a clear increase of f_{r}. This response proves that the previous hybridization of target and probe molecules as well as their immobilization was at least partially successful.

The concrete application of the sensor for gene detection is demonstrated with the next process steps: the device is immersed into solution with complementary ssDNA molecules. As described above, on-chip hybridization of the immobilized probe molecules occurs (*OCH dsDNA*). Following this process step the output signal exhibits a decrease of f_{r} and an increase of r_{shift}, as expected. However, in comparison to the first dsDNA immobilization process we generally observe a stronger response for the on-chip hybridization process (*OCH dsDNA*). This difference may indicate that a certain part of the immobilized DNA molecules are single stranded. On the other hand, Peterlinz and co-workers have observed that denaturation of immobilized dsDNA by heating can lead to an increase of the number of hybridizable probe molecules, possibly due to a reorganization of probe molecules during thermal treatment [40].

In the next step the hybridized DNA is denaturized again (*ssDNA*). In order to test the influence of the buffer solution used for hybridization to the measurement signal, the resonator is exposed to pure TE-NaCl buffer solution without DNA (*Buffer*). The data of these final process steps show some smaller random deviations from the reference data. The absolute values of r_{shift} (*ssDNA*) and r_{shift} (*Buffer*) represent a measure for the error signal of the system. The much more pronounced frequency shifts, however, can clearly be assigned to the detected DNA molecules. The functionalized sensor area is about 0.27 mm^2 including the coupling lines up to the PC switches. The surface density of thiol-modified 25-mer ssDNA oligo strands immobilized on gold has been measured by Peterlinz to be 9×10^{10} mm^{-2} (150 fmol mm^{-2}) [40]. We assume that our molecule surface density is rather lower, because the immobilized 20 b long dsDNA molecules have nearly twice the size. Taking the data of Peterlinz *et al* as an upper estimate, we calculate a maximum number of 40 fmol of DNA molecules or 4.8×10^{11} bp per resonator. The mass of the detected DNA molecules is approximately 2 ng. The sensitivity of the resonator—defined as relative frequency shift per base pair $r_{\text{shift/bp}}$—is 2.8×10^{-14} at maximum. The sensitivity of this waveguide-based resonant probing concept is more than five orders of magnitude higher than the previous free-space transmission configuration [36].

3.1.2. Disposable corrugated filter sensor chips. The sensitivity of resonant probing is mainly determined by the quality factor Q of the resonator. One basic requirement to increase the quality factor of a waveguide-based resonator is to reduce the internal propagation losses within the resonator cavity. The parallel-plate (PP) waveguide used for the sensing device concept presented in this section has an attenuation level which is approximately tenfold lower compared to the thin-film microstrip lines of the ring resonators demonstrated previously in this paper [32], enabling the development of sensors with much higher sensitivity. Beside sensitivity other aspects, e.g. costs, also play an important role for taking this technique from an essentially scientific development into a mature technology platform. Assuming one-way usage, a disadvantage of the fully integrated sensor chip presented above is high fabrication costs. An efficient way to reduce the running cost of this technique is based on separating the costly active generator/detector components for permanent use from the much cheaper passive biosensing resonator for one-way disposable application. The parallel-plate waveguide geometry enables modular coupling of different THz components with high positioning tolerance and broadband impedance matching with only minimal transition loss. In the following, two different fabrication methods for PP waveguide resonator chips are compared.

The applied configuration is sketched in figure 6. It consists of four separable components: a PP wave emitter, a PP wave detector, a flat metallized silicon chip and a metallized silicon chip with a corrugated surface used as photonic resonator in flip-chip configuration. Both emitter and detector chips are based on the same PP waveguide and comprise identical integrated structures: a Yagi-Uda slot-antenna launcher with coplanar waveguide feeding lines [41] embedded into a PP waveguide. The launcher consists of a $\lambda/2$-dipole element with a length of 185 μm. A photoconductive LT-GaAs switch is integrated into the feed-line at a 40 μm distance from the dipole of the antenna. For THz generation the switch is biased with 20 V and excited with optical pulses. For detector use, the feed-line is connected to a current amplifier to detect the photocurrent generated by an incoming PP wave signal. The launchers provide a 3 dB bandwidth of 105 GHz around a centre frequency of 470 GHz. The PP waveguide builds the basis for these components. It consists of a metallized silicon substrate with a 125 μm thick metallized polyester (PET) layer as dielectric on top. The resonator chip is the sensing device that will be functionalized with covalently bound DNA single strands for gene detection. It is equipped with a gold metallization and can therefore be applied for thiol-modified DNA

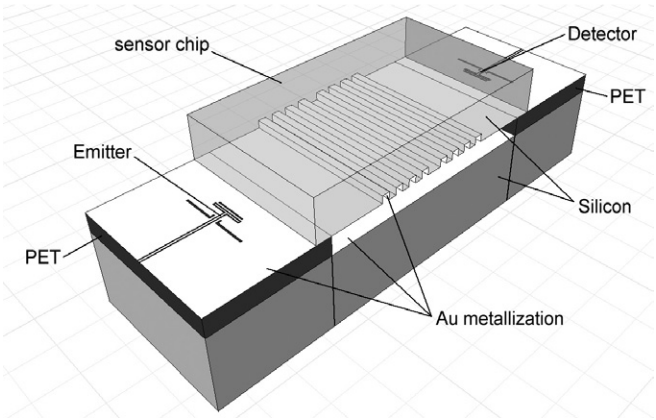

Figure 6. Schematic drawing of the THz transceiver system based on parallel-plate waveguide components.

binding as described above. The resonator concept used here corresponds to corrugated filters based on rectangular waveguides that are widely used at microwave frequencies [42]. We apply PP waveguides to this filter concept, because in comparison to rectangular waveguides they support broadband pulse transmission with negligible dispersion. The periodic corrugation generates a band-stop behaviour of the waveguide. Maximum attenuation is observed for free-space wavelengths λ fulfilling the Bragg-reflection condition $2p = n\lambda$, with p being the periodic distance of grooves. A defect in periodicity, on the other hand, generates a narrow-band resonance within the stop-band. The system is verified and optimized with numerical 3D-field-simulation software based on the finite element method (FEM) [43].

As sketched in figure 6, the complete transceiver system is configured by placing the detector and receiver chip in opposite directions with a metallized silicon substrate in between. The resonator is added in flip-chip configuration as a bridge between the outer components. Impedance mismatch ΔZ_0 between the dielectric-filled PP waveguides of the outer components and the air-filled waveguide of the resonator is $\Delta Z_0 = \varepsilon_r(\mathrm{PET})^{-1/2}$, with $\varepsilon_r(\mathrm{PET}) = 3.2$. Based on FEM simulations an insertion loss of less than 0.4 dB in the investigated frequency range of 0.3–0.8 THz is calculated for the transition. The geometry of the CPW feed-line is designed to exhibit strong high-frequency attenuation, effectively reducing disturbing signal reflections from the open ends.

The fabrication technology of the corrugated resonator chip has to fulfil the following main requirements: first, the geometry of the resonator design model should be reproduced as close as possible. Deviations in shape and scaling should be negligible or at least systematically reproducible in order to achieve the same transmission behaviour for every resonator. Secondly, the fabrication and material cost should be low. The technology should be generally applicable for high-volume production of one-way disposable sensor chips as well.

The dimensions of the corrugations scale with the wavelengths of the target frequency range. At THz frequencies structure sizes of passive components are normally in the range of several tens of micrometres. Several different fabrication technologies can be considered for THz devices [44]. Here, we compare two methods for fabrication of corrugated surfaces on silicon substrates: micro-machining and anisotropic wet etching. For micro-machining a wafer dicing saw (Disco, model DAD 321) is applied to cut rectangular grooves with a defined depth t into the surface of the silicon wafer. The grooves are arranged at a periodic distance p except for a defect distance d in the centre of the corrugation. The wafer saw has a

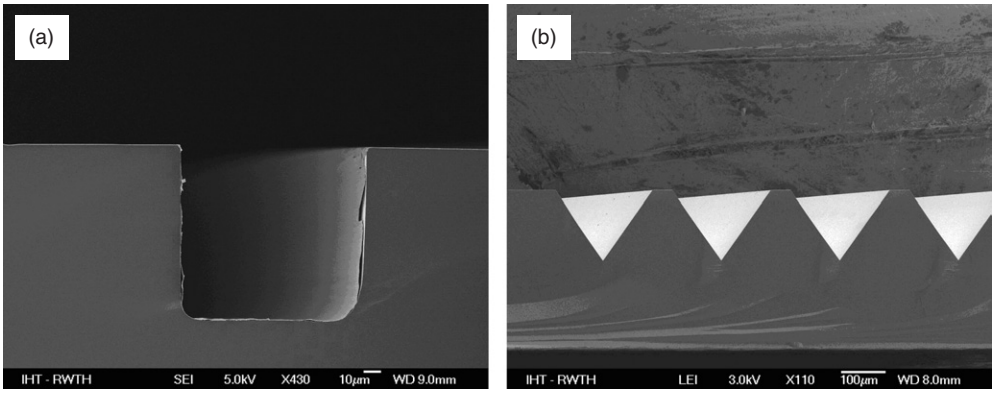

Figure 7. SEM pictures of the corrugated resonator chips fabricated using (a) micro-machining and (b) anisotropic wet etching. The micro-machined structure is metallized.

positioning tolerance of 1 μm. The width g of the grooves is directly defined by the width of the dicing blade. Anisotropic chemical wet etching is applied to structure v-shaped grooves. Using FEM simulations an intrinsic advantage of v-shaped corrugations in comparison to rectangular corrugations is observed: higher Q-factors can be achieved at identical transmission loss levels. The opening angle of 70.6° is defined by the crystal planes of the silicon substrate with (100) orientation. Therefore, the ratio g/t is always constant for this type of corrugation. The fabrication steps of the wet-etching process are as follows: after a cleaning step a 1 μm thick SiO_2 mask layer is deposited via thermal oxidation at 1050 °C. A photo-resist layer is spin-deposited and the groove structure is patterned into this soft mask layer. Then the groove pattern is transferred into the SiO_2 layer by wet etching in AF(NH_4F) acid solution. The v-grooves are defined in the last step: the uncovered silicon area is etched in KOH solution. As a result of anisotropic etching rates on (100)-oriented silicon, v-grooves with the mentioned angle develop. E-beam evaporated Cr and Au layers (10 nm and 300 nm, respectively) are deposited on every corrugated surface as metallization.

Pictures of the fabricated structures taken with a scanning electron microscope (SEM) are shown in figure 7. The most distinct deviations from an idealized geometry are observed for the micro-machining process. The profile of the dicing blade is not perfectly rectangular. Therefore, curvatures with radii between 5 and 15 μm appear at the bottom edges of the micro-machined grooves. Additionally, disruptions in the order of some microns occur at the upper edges of the grooves. The attrition of the dicing blade is giving rise to very fine random corrugations at the side wall surfaces of the grooves leading to cracks in the metallization layer. The highest degree in reproducibility and controllability is achieved with the anisotropic wet-etching technology. The low etching rate of silicon (1.37 μm min^{-1}) results in 117 min of etching time, which can be controlled very easily. Hence, the statistical spread in geometric dimensions (about 1–2 μm for v-groove fabrication) is mainly influenced by the lateral tolerance of the masking layer.

The resonators are characterized with the optoelectronic measurement system as described above. Following a Fourier transformation of the time-resolved measurement data, the transmission parameter S_{21} of the resonators is deduced by normalizing the transmitted signal to a reference signal measured with a flat resonator section. This normalization procedure is very useful to correct for all spectral dependences of the measurement system, emitter and detector—it only neglects the very small attenuation (approximately 0.03 dB mm^{-1}) of the flat PP waveguide. A comparison of the measured and simulated resonator transmission

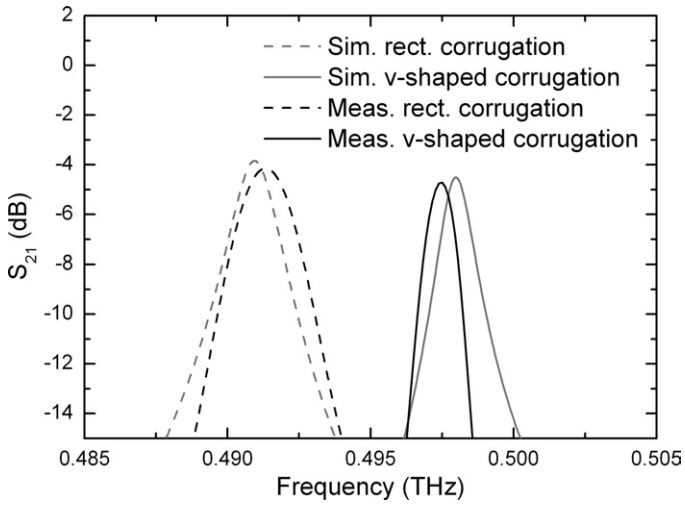

Figure 8. Comparison of measured and simulated transmission parameter S_{21} of resonators with rectangular and v-groove corrugation. Grey curves show simulated data.

Table 1. Measured and simulated centre resonance frequency f_r, Q-factor and insertion loss S_{21} for the rectangular and v-groove corrugated resonator.

	f_r meas. (GHz)	f_r sim. (GHz)	Q meas.	Q sim.	$S_{21}(f_r)$ (dB) meas.	$S_{21}(f_r)$ (dB) sim.
Rect. groove	491.3	491.0	209	273	−4.2	−3.8
v-groove	497.5	498.0	436	400	−4.7	−4.5

parameter S_{21} is depicted in figure 8. In table 1 the key parameters of the resonators extracted from transmission data are listed for comparison. There is generally a good agreement between measurement and simulation data. The best agreement is observed for the v-groove corrugated structure fabricated with chemical wet etching (process (c)). We measure a very high Q-factor of 436 at a still reasonable insertion loss of −4.7 dB. The quality factors achieved in this PP waveguide configuration are a drastic improvement in comparison to TFMS line based ring resonators with a demonstrated $Q = 50$ at 245 GHz. A significant increase in sensitivity is therefore expected. It is important to note that the measured and simulated loaded Q-factors described above represent the quality factor of the *coupled* resonator, i.e. of the resonator connected to the signal generation and detection modules. Coupling is equivalent to a resonator loss mechanism, degrading the *intrinsic* resonator Q in proportion to the strength of the coupling parameters. As coupling factors are a free design parameter, it is interesting to estimate therefore also the maximum Q-factor value achievable of the intrinsic resonance of the decoupled resonator. FEM calculations indicate an intrinsic unloaded Q-factor for the v-groove structure of more than 1000.

The number of essential fabrication steps for micro-machining and wet etching are two and six, respectively. The micro-machining process exhibits good results in terms of reproducibility, scalability and performance. Anisotropic wet etching of v-groove corrugations, however, is the fabrication technology with the highest quality in this comparison enabling the most perfect structures with very high reproducibility. Additionally, v-shaped corrugations intrinsically exhibit higher electromagnetic performance in comparison to rectangular shaped corrugations. Considering mass production compatibility, anisotropic wet etching might be more attractive than micro-machining.

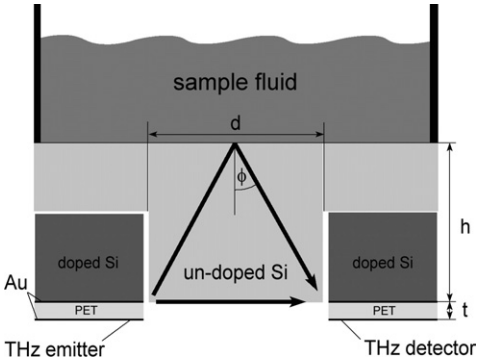

Figure 9. Schematic cross-section of the integrated transceiver system for spectroscopy and biosensing of fluidic samples. The plotted parameters are $\Phi = 33°$, $d = 1.3$ mm, $h = 1.0$ mm and $t = 0.125$ mm.

3.1.3. Integrated fluidic THz-sensor device. The majority of THz spectroscopy investigations on biomolecules are performed on dried samples. Since water exhibits extremely high absorption within the THz range (about 240 cm^{-1} at 1 THz), transmission experiments and resonant approaches for biomolecule sensing are becoming impractical in aqueous solutions. For example, a transmission signal can hardly be detected at the previously demonstrated waveguide-based resonators applied to water solutions. However, analysis of biomolecules in liquids is highly desirable since the functionality of delicate molecules like proteins or RNA often depends on appropriate suspension and biochemical processes normally only take place in solution, as well. For the mentioned reasons, spectroscopy of water on its own is a challenging task at THz frequencies. Water and water-based solutions were measured in transmission and in reflection configurations. In order to reduce signal path length and, hence, THz signal attenuation in transmission experiments thin chambers have been applied [45, 46]. Reflection mode configurations [47], however, proved to be preferable for dielectric characterization of highly absorbing matter because the dynamic range available is higher in comparison to transmission mode [48]. In the following, a compact integrated transceiver system for THz spectroscopy and biosensing applications is introduced. Like the transceiver system for resonator characterization it is based on directly coupled emitter, transducer and detector components. The system is especially useful for investigations at strongly absorbing fluids because the sample is probed in reflection configuration. In comparison to standard free-space transmission systems the integrated system offers drastically reduced space requirements, strongly reduced effort in adjustment and a higher SNR due to efficient signal coupling.

The cross-section of the measurement system is shown in figure 9. Photoconductive Yagi–Uda antennas embedded into a PP waveguide—as used for PP resonator characterization (figure 6)—are applied as THz emitter and detector devices. In this case the transmitted THz signal is not coupled into an intermediate waveguide structure but partly radiated into a block of undoped silicon with a length of $d = 1.3$ mm and a height $h = 1.0$ mm. The undoped silicon is part of the bottom of a reservoir containing the sample fluid. Two signal paths as sketched in figure 9 are considered for our measurement: a signal reflected at the silicon/sample interface and a directly transmitted signal not interacting with the sample. The geometric scaling of the intermediate silicon introduces a path length difference that is large enough for time-domain separation of both signal components. Because the directly transmitted signal does not contain any information about the sample it can be used as a reference signal and to correct for possible drifts in optical excitation power between different measurements. Owing to the

PP waveguide emitter the THz signal is polarized in the parallel direction to the reflection plane. The principle of using this system for detecting biomolecules in solution is based on diverse dielectric THz properties of solvent (e.g. pure water) and solute sample molecules. In order to increase the sample molecule concentration at the reflection surface, and hence sensitivity, it can be functionalized with highly selective capturing molecules. The natural oxide on silicon is an excellent surface for functionalization with DNA strands [49], for example. Maximum sensitivity to dielectric changes of the sample solution can be expected for incident angles close to the critical angle of total reflection. Following Snell's law, with a refractive index $n = 3.42$ for undoped silicon and the incident angle $\Phi = 33°$ used in our configuration maximum sensitivity will be achieved at samples with refractive index $n = 1.86$.

In a first demonstration the fluidic THz-sensor device is applied to water–ethanol mixtures monitoring the complex dielectric constant under variation of ethanol molarity in a range of 0–100%. Water–alcohol solutions are very interesting under biological aspects: hydrophobic hydration is commonly regarded as one of the most important effects influencing the structural stability of proteins. However, the molecular dynamics of hydrophobic hydration are still not completely understood. Water–alcohol mixtures offer a basic system where competing hydration processes of polar and non-polar hydrogen-bonding groups can be studied theoretically [50] and experimentally [51]. THz technology already proved to be a very useful completion of the numerous measurement tools available in the frequency ranges below [52] and above [51, 53, 54] the THz range. It has been applied to dielectric relaxation measurements of nonpolar [55] and polar liquids [56] and nonpolar–polar liquid mixtures [57]. Pure water is characterized by a network of H-bonded molecules. Upon the addition of alcohol disconnected clusters of water and alcohol molecules appear [58]. Valuable information can be revealed from THz measurements, since e.g. the hydrogen bond strength of water and alcohol molecules fluctuates rapidly with characteristic THz-range correlation times τ of 0.1–1 ps [52]. Recently, water–ethanol mixtures have been dielectrically characterized with THz transmission spectroscopy [46]. In this study the molarity of EtOH was varied with rather large increments of 20%. In order to locate concentration-dependent abnormalities of the water–ethanol mixture more precisely, however, a much higher molarity resolution is clearly desirable, as demonstrated by microwave range measurements [59]. Our system offers direct access to the sample fluid as well as high SNR. Therefore, large series of measurements with small increments of concentration can be easily made in a short time.

Exemplary time-domain data measured at the fluidic sensor device are depicted in figure 10 for the empty sensor and the sensor filled with H_2O or EtOH. The measured signals are characterized by two wave packages: the first wave package stems from the direct transmission pathway, the second one originates from the reflected signal. In addition to the geometrical pathway difference between both signals there is additional retardation of the reflected signal due to the refractive index of silicon. The peak amplitude of the directly transmitted signal is defined as time delay $t = 0$ ps. Upon application of sample fluid no influence on the transmitted signal can be observed for time delays up to $t = 15.8$ ps. For $t > 15.8$ ps the second wave package is detected showing distinct amplitude and phase modulation in comparison to the reference signal following the application of water or ethanol. From time domain data of the reflected signal we calculate the Fresnel coefficient of the complex reflectivity $\hat{r}_s = R_s \times e^{i\theta_s}$ of the silicon–sample interface under assumption of plane wave excitation by

$$\hat{r}_s = r_{ref} \frac{\hat{E}_s(f)}{\hat{E}_{ref}(f)}, \tag{4}$$

where r_{ref} is the reflectivity of the silicon–air interface and $\hat{E}_s(f)$ and $\hat{E}_{ref}(f)$ the complex Fourier-transformed data of the reflected signal measured at the sample and the empty sensor,

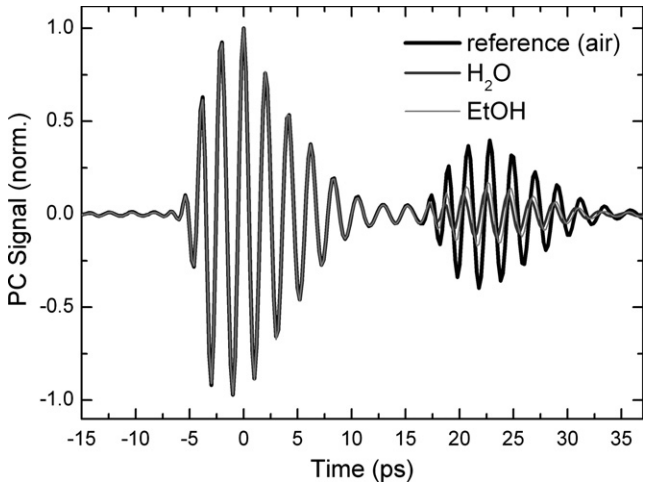

Figure 10. Time-resolved measurement data of the THz signal transmitted through the fluidic sensor device for an empty reservoir (reference), pure water and ethanol.

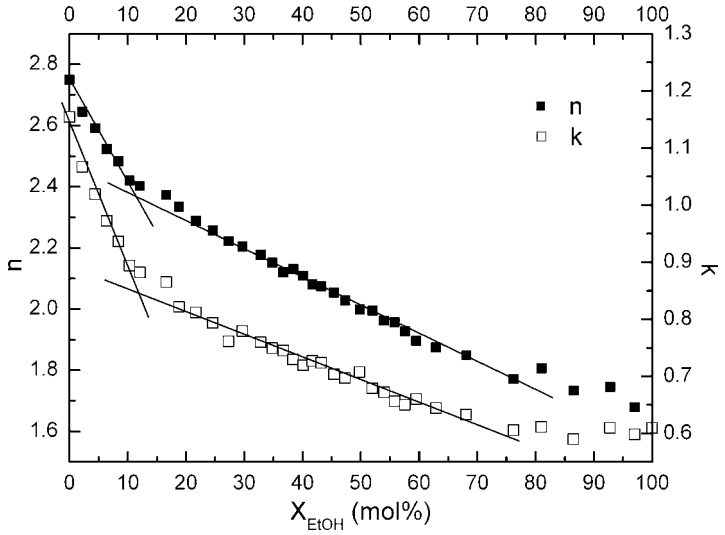

Figure 11. Real and imaginary part of the dielectric refractive index n and k at $f = 0.5$ THz calculated from the Fourier-transformed measurement data for different ethanol molarities X_{EtOH} (mol%). The straight lines are guides to the eyes.

respectively. From $\hat{r}_{\mathrm{s}}$ the complex refractive index $\hat{n}_{\mathrm{s}} = n_{\mathrm{s}} - \mathrm{i}k_{\mathrm{s}}$ of the sample solution has been calculated numerically for non-normal incidence using a similar approach as in [60].

We measured the dielectric behaviour of water–ethanol mixtures with increments of ethanol molarity X_{EtOH} around 2–6% in a range of 0–100%. First, the sensor was filled with water. Following each THz signal measurement X_{EtOH} was increased stepwise up to 40%. Then the reservoir was emptied, dried and filled with ethanol. After this step X_{EtOH} was decreased and measured in the same way down to 40%. Real and imaginary parts of the complex dielectric refractive index $\hat{n}_{\mathrm{s}}(X_{\mathrm{EtOH}})$ are plotted for frequency $f = 0.5$ THz in figure 11. Both n and k are more or less monotonically decreasing with X_{EtOH}. The most

salient feature in both curves is the change of gradient at $X_{\mathrm{EtOH}} = 10\%$. At this molarity an absolute maximum of H-bonds per water molecule has been identified using molecular dynamics simulation [61]. In an ideal water–ethanol mixture the number of H-bonds per water molecule would decrease linearly with X_{EtOH}. The increase of water H-bonds for low ethanol concentrations is therefore a typical anomalous mixture behaviour which is commonly attributed to hydrophobic hydration [62]. The evaluation of dielectric data used here is based on the assumption of a plane wave excitation. The PP waveguide coupling sections as well as the relatively close distance of the emitter and detector components might have a negative influence on the validity of this assumption. Nevertheless, our data is showing good qualitative agreement with previous data from transmission-mode measurements [46]. In order to increase the absolute accuracy of dielectric parameter extraction further 3D numerical field simulation of the device structure will be applied in a next step.

4. Summary

In conclusion, we have presented different concepts of integrated THz-sensor devices for marker-free biosensing applications. Functionalized resonators have been demonstrated to detect specific DNA sequences at probe molecules immobilized on the sensor surface via time-resolved photoconductive sampling technique with femtomole sensitivity. This principle is suitable for the parallel execution of several hybridizing experiments on a chip with an array arrangement of differently functionalized sensors. A compact THz transceiver device for fluidic analysis has been introduced and applied for the characterization of water–ethanol mixtures. The implementation of asynchronous optical sampling into the biochip reader system is an important development step that strongly increases the data throughput for this type of sensing devices.

Acknowledgments

We gratefully acknowledge financial support by the Deutsche Forschungsgemeinschaft (DFG) and by the European Commission. We also thank our former colleagues H-M Heiliger, M Brucherseifer, T Dekorsy, F Richter and P Haring Bolivar for providing us with an excellent basis for this work, A Marchewka for conducting fluidic measurements and M Elwert for fabricating corrugated THz resonator chips.

References

[1] Siegel P H 2004 *IEEE Trans. Microw. Theory Tech.* **52** 2438–47
[2] Lawrence A F, McDaniel J C, Chang D B and Birge R R 1987 *Biophys. J.* **51** 785–93
[3] Van Zandt L L and Saxena V K 1989 *Phys. Rev.* A **39** 2672–4
[4] Markelz A, Whitmore S, Hillebrecht J and Birge R 2002 *Phys. Med. Biol.* **47** 3797–805
[5] Mickan S P *et al* 2002 *Phys. Med. Biol.* **47** 3789–95
[6] Nagel M, Richter F, Haring Bolivar P and Kurz H 2003 *Phys. Med. Biol.* **48** 3625–36
[7] Woodward R M, Wallace V P, Arnone D D, Linfield E H and Pepper M 2003 *J. Biol. Phys.* **29** 257–61
[8] Schmuttenmaer C A 2004 *Chem. Rev.* **104** 1759–79
[9] Dragoman D and Dragoman M 2004 *Prog. Quantum Electron.* **28** 1–66
[10] Leitenstorfer A, Hunsche S, Shah J, Nuss M C and Knox W H 1999 *Appl. Phys. Lett.* **74** 1516–8
[11] Huber R, Brodschelm A, Tauser F and Leitenstorfer A 2000 *Appl. Phys. Lett.* **76** 3191–3
[12] Zhang X-C and Auston D H 1992 *J. Appl. Phys.* **71** 326–38
[13] Auston D H 1983 *IEEE J. Quantum Electron.* **19** 639
[14] Auston D H, Cheung K P and Smith P R 1984 *Appl. Phys. Lett.* **45** 284–6

[15] Heiliger H M *et al* 1997 *Appl. Phys. Lett.* **70** 2233–5
[16] Ludwig C and Kuhl J 1996 *Appl. Phys. Lett.* **69** 1194–6
[17] Heiliger H M, Vosseburger M, Roskos H G, Kurz H, Hey R and Ploog K 1996 *Appl. Phys. Lett.* **69** 2903–5
[18] Segschneider G, Dekorsy T, Kurz H, Hey R and Ploog K 1997 *Appl. Phys. Lett.* **71** 2779–81
[19] Beard M C, Turner G M and Schmuttenmaer C A 2001 *J. Appl. Phys.* **90** 5915–23
[20] Nemec H, Pashkin A, Kuzel P, Khazan M, Schnüll S and Wilke I 2001 *J. Appl. Phys.* **90** 1303–6
[21] Rosker M J, Wise F W and Tang C L 1986 *Phys. Rev. Lett.* **57** 321–4
[22] Kwong K F, Yankelevich D, Chu K C, Heritage J P and Dienes A 1993 *Opt. Lett.* **18** 558–60
[23] Lai M 2001 *Appl. Opt.* **40** 6334–6
[24] Xu J and Zhang X-C 2004 *Opt. Lett.* **30** 2082–4
[25] Elzinga P A, Kneisler R J, Lytle F E, Jiang Y, King G B and Laurendeau N M 1987 *Appl. Opt.* **26** 4303–9
Kneisler R J, Lytle F E, Fiechtner G J, Jiang Y, King G B and Laurendeau N M 1989 *Opt. Lett.* **14** 260–2
[26] Kafka J D, Pieterse J W and Watts M L 1992 *Opt. Lett.* **17** 1286–8
[27] Keilmann F, Gohle C and Holzwarth R 2004 *Opt. Lett.* **29** 1542–4
[28] Adachi S, Takeyama A and Takagi Y 1995 *Opt. Commun.* **117** 71–7
[29] Janke C, Först M, Nagel M, Kurz H and Bartels A 2005 *Opt. Lett.* **30** 1405–7
[30] Bartels A, Dekorsy T and Kurz H 1999 *Opt. Lett.* **24** 996–8
[31] Nagel M, Dekorsy T and Kurz H 2002 *European Patent Specification* EP 1205005
[32] Mendis R and Grischkowsky D 2001 *IEEE Microw. Wir. Comp. Lett.* **11** 444–6
[33] Nagel M *et al* 2002 *Appl. Phys. Lett.* **80** 154–6
[34] Ozaki H and McLaughlin L W 1992 *Nucleic Acids Res.* **20** 5205–14
[35] Zhuang W, Feng Y and Prohofsky E W 1990 *Phys. Rev.* A **41** 7033–42
[36] Brucherseifer M *et al* 2000 *Appl. Phys. Lett.* **77** 4049–51
[37] Curtis J A and Fiedziuszko S J 1991 *IEEE MTT-S Int. Microw. Symp. Dig.* **2** 443–6
[38] Himmel HJ, Terfort A, Arnold R and Wöll C 1999 *Mater. Sci. Eng.* C **8/9** 431–5
[39] Herne T M and Tarlov M J 1997 *J. Am. Chem. Soc.* **119** 8916–20
[40] Peterlinz K A, Georgiadis R A, Herne T M and Tarlov M J 1997 *J. Am. Chem. Soc.* **119** 3401–2
[41] Hammad H F *et al* 2003 *IEEE Trans. Microw. Theory Tech.* **51** 1234–40
[42] Levy R 1973 *IEEE Trans. Microw. Theory Tech.* **21** 526–32
[43] *HFSS 9.2.1* Ansoft Corporation, Pittsburgh, PA
[44] Biber S, Schur J, Hofmann A and Schmidt L P 2004 *IEEE MSMW04 Symp. Proc. (Kharkov, Ukraine)* pp 21–6
[45] Mickan S P, Shvartsman R, Munch J, Zhang X-C and Abbott D 2004 *J. Opt. B: Quantum Semiclass. Opt.* **6** 786–95
[46] Kitahara H, Yagi T, Mano K, Takeda M W and Nishizawa S 2005 *J. Korean Phys. Soc.* **46** 82–5
[47] Thrane L, Jacobsen R H, Uhd Jepsen P and Keiding S R 1995 *Chem. Phys. Lett.* **240** 330–3
[48] Jepsen P U and Fischer B M 2005 *Opt. Lett.* **30** 29–31
[49] Chrisey L A, Lee G U and O'Ferrall C E 1996 *Nucleic Acids Res.* **24** 3031–9
[50] Allison S K, Fox J P, Hargreaves R and Bates S P 2005 *Phys. Rev.* B **71** 024201–5
[51] Dixit S, Crain J, Poon W C K, Finney J L and Soper A K 2002 *Nature* **416** 829–32
[52] Kaatze U 2000 *Subs. Sens. Tech. Appl.* **1** 377–91
[53] Liddel U and Becker E 1957 *Spectrochim. Acta* **10** 70–84
[54] Vahvaselka K S, Serimaa R and Torkkelli M J 1995 *Appl. Crystallogr.* **28** 189–95
[55] Pedersen J E and Keiding S R 1992 *IEEE J. Quantum Electron.* **28** 2518–22
[56] Kindt J T and Schmuttenmaer C A 1996 *J. Phys. Chem.* **100** 10373–9
[57] Venables D S and Schmuttenmaer C A 1998 *J. Chem. Phys.* **108** 4935–44
[58] Koga Y, Nishikawa K and Westh P 2004 *J. Phys. Chem.* A **108** 3873–7
[59] Sato T, Chiba A and Nozaki R 1999 *J. Chem. Phys.* **110** 2508–21
[60] Rønne C 2000 Intermolecular liquids dynamics studied by THz spectroscopy *PhD Thesis* University Aarhus
[61] Noskov S Y, Lamoureux G and Roux B 2005 *J. Phys. Chem.* B **109** 6705–13
[62] Onori G and Santucci A 1996 *Mol. Liq.* **69** 161–81